Intracellular mechanical fingerprint reveals cell type specific mechanical tuning

Till M. Muenker[1,2*], Bart E. Vos[1,2], and Timo Betz[1,2]

[1] *Third Institute of Physics, Georg August Universität Göttingen, Göttingen, Germany*

[2] *Cluster of Excellence 'Multiscale Bioimaging: From Molecular Machines to Networks of Excitable Cells' (MBExC), Georg August Universität Göttingen, Göttingen, Germany*

[*] *Corresponding author*

Abstract

Living cells are complex entities that perform many different complex tasks with astonishing robustness. While the direct dependence of biological processes on controlled protein expression is well established, we only begin to understand how intracellular mechanical characteristics guide and support biological function. This is in stark contrast to the expected functional role that intracellular mechanical properties should have for many core cellular functions such as organization, homeostasis and transport. From a mechanical point of view, cells are complex viscoelastic materials that are continuously driven out of thermodynamic equilibrium, which makes both a physical measurement and mathematical modeling of its properties difficult. Here, we define a "mechanical fingerprint" that can not only characterize the intracellular mechanical state, but also carve out the mechanical differences between cell types with the potential to relate these to proper cell function. By analyzing the frequency-dependent viscoelastic properties and intracellular activity of cells using microrheology, we distilled the complex active mechanical state into just 6 parameters that comprise the mechanical fingerprint. The systematic investigation of the fingerprint illustrates a parameter tuning that can be explained by the functional cellular requirements. However, the full potential of the mechanical fingerprint is given by a statistical analysis of its parameters across all investigated cell types, which suggests that cells adjust mechanical parameters in a correlated way to position their intracellular mechanical properties within a well defined phase-space that is spanned between activity, mechanical resistance and fluidity. This paves the way for a systematic study of the interdependence of biological function and intracellular active mechanics.

Main

Introduction

Cells are highly complex, heterogeneous materials that tightly control their viscoelastic characteristics by precise tuning of the active mechanical properties to maintain a non-equilibrium mechanical steady state. This mechanical homeostasis requires a continuous consumption of metabolic energy, mostly in the form of ATP and is maintained while the system undergoes various dynamic functions ranging from tissue morphogenesis and patterning[1,2] to organelle positioning,[3] differentiation,[4] migration[5,6] and polarization.[7]

Although it is well-acknowledged that intracellular mechanical properties are key to understanding major cellular functions, most studies have measured cellular mechanics from outside of the cell using e.g. AFM,[8,9] micropipette aspiration,[10] traction force microscopy,[11] tether pulling,[12] magnetic twisting cytometry[13] or deformability cytometry.[14] While these studies allowed deep insights into the relevance of cell mechanics for supracellular biological processes by probing predominantly the stiff actin cortex that surrounds the cell, inferring information about the cytoplasm mechanics remained difficult.[15] This experimental gap has recently been bridged by active intracellular rheology experiments that are based on optical as well as magnetic tweezers.[16–19] For example, a recent study has shown that the cytoplasm is softening during mitosis[20] which might be key for the proper functioning of this process.

While a large body of work has focused on the viscoelastic properties of cells, it became increasingly clear that the well-controlled active force generation of living cells has to be integrated to obtain a full intracellular mechanical description. A multitude of recent studies has therefore focused on investigating these non-equilibrium, active properties of cells.[21–23] These active, energy consuming cellular processes are a key component to maintain the intracellular organization despite the ever-dispersing forces of entropy.[16,24] While the intracellular transport continuously organizes membrane and organelle architecture via motor activity, the dynamic growth and disassembly of cytoskeletal filaments ensures global processes such as migration,[25] proliferation[26] or wound healing.[27] Further, recent studies have shown that dynamic waves of actin filaments also organize mitochondria position during cell division[28] and that cytoplasmic forces can reorganize nuclear condensates,[29] thus emphasizing the key importance of active forces for fundamental cellular function.

Despite the generally accepted relevance of intracellular active mechanics for the functioning of entire organisms, it remains difficult to quantify and even harder to model theoretically. From a physical perspective, cells behave as viscoelastic materials where timescales are a key information to correctly identify the dominating mechanical principles. Therefore, a full quantitative description requires microrheological information, typically provided in the form of a frequency dependent, complex shear modulus $G^*(f)$.[30] Although this quantification of the viscoelasticity is experimentally accessible, its interpretation requires theoretical models to become physically meaningful and to reduce the complexity of data. However, while simple mechanical anologies such as Kelvin-Voigt or Maxwell models lack the complexity to

describe the observed behaviour, more elaborate models such as chains of springs and dashpots require many parameters and thus do not reduce the complexity significantly. This has led to double power law approaches, that are motivated by fractional Generalized Kelvin-Voigt (fGKV) models.[31] In recent work these have been successfully used to quantify the viscoelastic properties of fibroblasts,[32] endothelial[33] and epithelial cells[20] and they reduce the complex mechanical behaviour to just four parameters. Recent efforts to include the active force generation in a mechanical characterization have been able to describe the active energy injected into the cellular system also by a power law[20] that is defined by two additional parameters.

These insights beg the question to which extent living cells actively control their intracellular mechanical properties, or if these are simply the byproduct of the cytoplasmic composition. Assuming a functional relevance, the parameters may vary considerably between cells, and might even allow to identify different cell types and cellular situations in a fingerprint-like fashion. The relevance of this 6 parameter description was recently established by showing systematic changes during cell division, and to perform new statistical analysis of stochastic particle trajectories.[20,34] In this study we use optical tweezers based active microrheology and passive observation of intracellular particle motion to demonstrate that cell types can be successfully distinguished in a pairwise comparison to position cells on 3D phasespace that reflects activity, rigidity and fluidity.

Mechanical parameter set quantifies active mechanics

Intracellular viscoelastic material properties are commonly quantified by a frequency-dependent, complex shear modulus that we directly determine via optical tweezers based active microrheology (M 2). Here, a custom-built optical tweezers setup (Figure 1a, M 1) exerts well-defined oscillatory forces onto phagocytosed 1 µm sized probe particles inside cervical cancer cells (HeLa). To determine the resulting bead displacement, a stationary, weak detection laser monitors the particle position with nanometer precision. Applying sinusoidal forces (Figure 1b) with frequencies between 1 Hz and 1024 Hz allows to calculate the mechanical response function $\chi(f)$, which is used to determine the complex shear modulus $G^*(f) = 1/(6\pi R\chi(f))$, with R the probe particle radius (Figure 1c). $G^*(f)$ is a complex quantity where the real part $G'(f)$ (storage modulus) describes the elastic properties of the cell and the imaginary part $G''(f)$ (loss modulus) describes the viscous properties (Figure 1c).

To model the shear modulus we follow the naive hypothesis that the cytoplasm consists of two main material classes, namely an elastic solid-like material that is generated by a sparse, connected polymer network, and a more liquid-like material that fills the bulk space of the cytoplasm (Figure 1d). Generally, such a combination of two complex materials can be approached by a linear combination of two springpots that leads to a double power law model consistent with classical rheology data[20,31–33] :

$$G^*(f) = A(2\pi i f)^\alpha + B(2\pi i f)^\beta \tag{1}$$

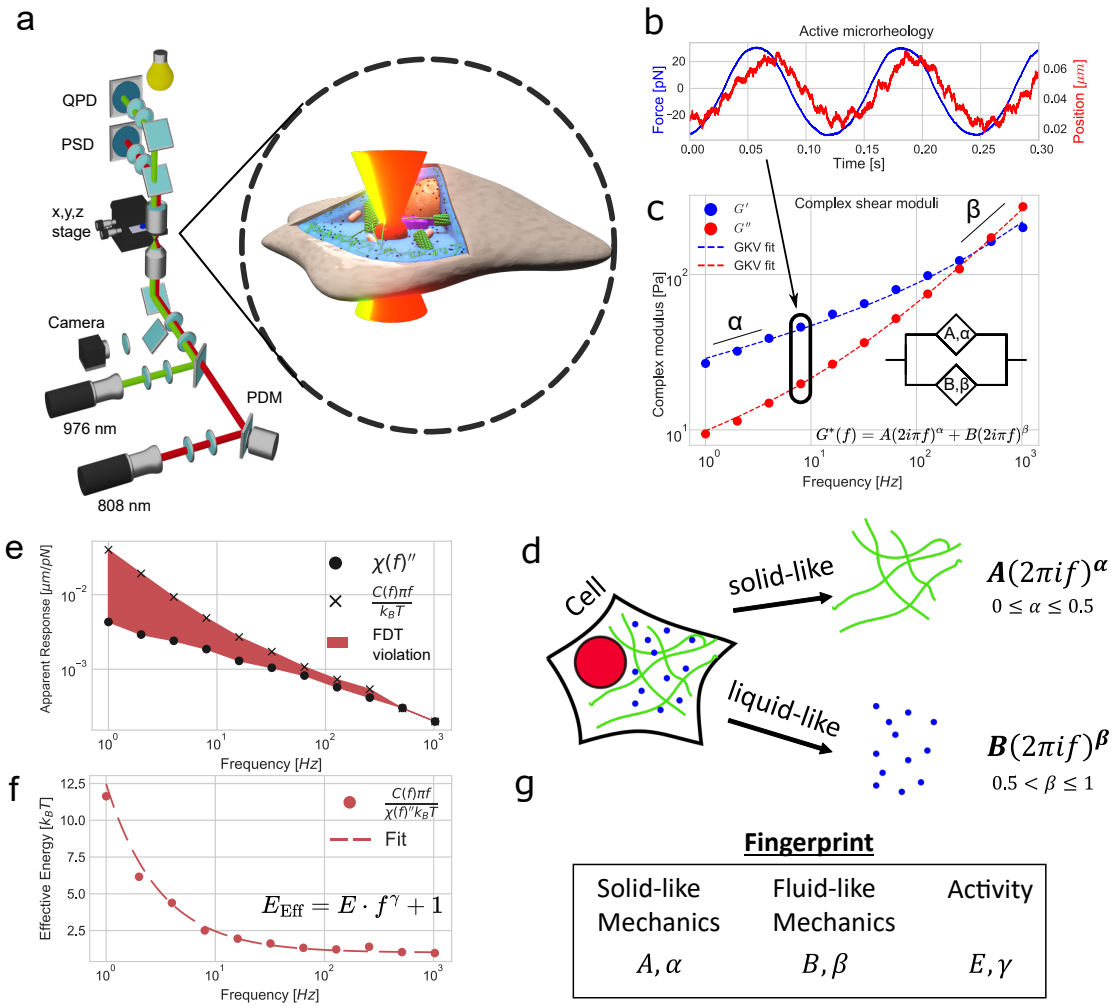

Figure 1: a) Viscoelastic properties and activity are measured within the cytoplasm of cells using a custom build optical tweezers setup. b) Sinusoidal forces (blue) at varying frequencies are applied to a probe particle while the particle displacement (red) in response to this force is monitored. c) Repeating this procedure at different frequencies allows to calculate viscoelastic material properties in terms of the complex shear modulus $G^*(f)$ which consists of the storage modulus (blue) and a loss modulus (red). Both storage and loss modulus can collectively be fitted using a generalized fractional Kelvin-Voigt (fGKV) model(inset). d) This fGKV model consists of two power laws which in a simplified way can be pictured as a more solid-like material class resembling polymeric filaments and a more fluid-like material class (crowded molecules). e) Using an additional passive measurement, violation of the fluctuation-dissipation theorem can be directly visualized. (red area) f) The effective energy quantifies intracellular activity and can be fitted with a two parameter power law. g) Complex and frequency dependent intracellular active mechanical properties can be reduced to a fingerprint of just 6 parameters, which describe the intracellular mechanical state.

This complex function can then be used to simultaneously fit both the real and imaginary part of the experimentally obtained shear modulus to determine the prefactors and power law exponents. As shown in Figure 1c the model fits the experimental data well. R^2-values of the fits are given for raw trajectories (Figure 2, Table 14) and bootstrapped trajectories (Figure 3, Table 16). Consistent with the initial hypothesis, we identify a region with an power law exponent between 0 and 0.5 that we attribute to a more solid-like material (ideal solid has exponent 0), and a second power law that is between 0.5 and 1 (ideal fluid has exponent 1) corresponding to a liquid-like material.

Besides intracellular mechanics, the generated active forces are another key determinant of the intracellular state. As cells consume metabolic energy to drive motor proteins and many other cell biological functions, cells are far from thermodynamic equilibrium. Experimentally, this is directly reflected in the motion of tracer particles within the cell. In thermodynamic equilibrium, the random motion of particles depends only on material properties and temperature, which is manifested by the fluctuation-dissipation theorem:[35]

$$C(f) = \frac{k_{\mathrm{B}} T \chi''(f)}{\pi f} \tag{2}$$

Here, $C(f)$ is the power spectral density, quantifying the spontaneous fluctuations of the particle, $\chi(f)$ is the mechanical response function and $k_{\mathrm{B}}T$ is the thermal energy. In active, living cells particle mobility is beyond motion explainable by thermal fluctuations[36] (Figure 1e), as cytoskeletal rearrangement and transport processes also contribute to the motion of probe particles. An elegant way to summarize all active and thermal forces is by introducing an effective energy E_{Eff}[35](M 2). Intuitively, this effective energy reflects the ratio between observed particle motion $C(f)$ thermodynamically predicted motion that reflect the dissipative material properties as quantified by $\chi''(f)$:

$$E_{\mathrm{Eff}}(f) = \frac{C(f)}{\chi''(f)} \frac{\pi f}{k_{\mathrm{B}} T} \tag{3}$$

It should be noted that this idea of an effective energy implies that the active forces generated by the cell share statistical characteristics with thermal forces. In this sense we use the effective energy rather as a phenomenological quantity that measures the extent of non-equilibrium mechanical driving of the system. The free particle fluctuation spectrum $C(f)$ is acquired by turning off the trapping laser while using the lower-power detection laser to monitor the particle position. The resulting average effective energy measured for HeLa cells (Figure 1f) shows an increase influence of active forces in the low frequency regime, while the effective energy converges to the thermal limit of 1 $k_{\mathrm{B}}T$ for higher frequencies. This is a direct demonstration that metabolic energy dominates slow particle motion, while assuming a thermodynamic equilibrium from shorter timescales is an adequate approximation. This asymptotic behaviour at short time scales is to be expected as motor proteins operate at longer time scales,[37] and has previously been shown experimentally.[16] Interestingly, this suggests that the question about non-equilibrium processes can be reduced to a question of timescales, which is a potential explanation why this subject is so controversially discussed in literature. This asymptotic behaviour

offers an additional calibration method of optical tweezers in complex living systems[35] that we used to optimize the readout of the effective energy and mechanical properties (see SI 1.1 for further discussion).

Similar to the mechanical properties, the effective energy can also be fit by a power law approach (Figure 1f):

$$E_{\mathrm{Eff}}(f) = Ef^{\gamma} + 1 \tag{4}$$

This enabled us to use only two parameters when quantifying all active forces injected in the cell by metabolic processes in a single description. In combination with the 4 parameters that are sufficient to describe the viscoelastic properties, we can establish a set of 6 parameters that fully describes the state of a cell, and in particular the active mechanics of the cytoplasm in HeLa cells (Figure 1f). As we show in the following, the set of these 6 parameters can be interpreted as mechanical fingerprint of a cell (Figure 1g).

In this study, we explore the variation of the mean active mechanical quantities G', G'', and E_{Eff} across different cell types or conditions. To obtain a robust and reliable distribution of these curves, we apply a bootstrapping scheme to the recorded single cell data (see M 3.1). The bootstrapped data is then subjected to respective model fitting, providing estimations for the distributions of the mean fingerprint parameters for each condition. Unless otherwise specified, all presented data is based on the bootstrapped data.

The cytoskeleton selectively affects the mechanical fingerprint

After verifying that HeLa cells are well described by the mechanical fingerprint, we wondered if different parameters can be affected by pharmacological perturbation of the cytoskeleton (Figure 2a). Commonly, the mechanical properties of cells are attributed to the actin cytoskeleton, which forms the cell cortex and other structures. Consequently, we disrupted the actin cytoskeleton in Hela cells using Cytochalasin B (CytoB or CB) and investigated the resulting fingerprint. To our surprise, we did not observe strong changes in intracellular active mechanics (Figure 2b-j grey). We solely observe a weak, yet significant decrease of solid-like exponent α (0.36 to 0.31). Neither the elastic modulus nor the viscous modulus of the cytoplasm (Figure 2h,i grey) is visibly affected by disruption of the actin cortex. As the probe particle is phagocytosed, it is rapidly transported away from the cell surface, and typically confined in a late endosome or lysosome. This can explain why the viscoelastic properties in terms of fingerprint parameters A, α, B and β experienced by the probe particle are mostly unaffected and why the effective energy remains unaffected (Figure 2 b-j grey). As the interaction of phagocytosed particles is mainly dominated by microtubule associated motor proteins, no effects of actin perturbation are expected. This explanation predicts that both, the effective energy and the viscoelastic material properties, should be affected when depolymerizing microtubules (MT). To test this prediction, we disrupted the MT network using $10\,\mu\mathrm{g}\,\mathrm{mL}^{-1}$ Nocodazole (Nocoda or Noc). As expected, the activity was almost completely abolished (Figure 2 c,g,j yellow) by this treatment as mainly captured by a drastic reduction of the effective energy defining prefactor E. Strikingly, even depolymerization

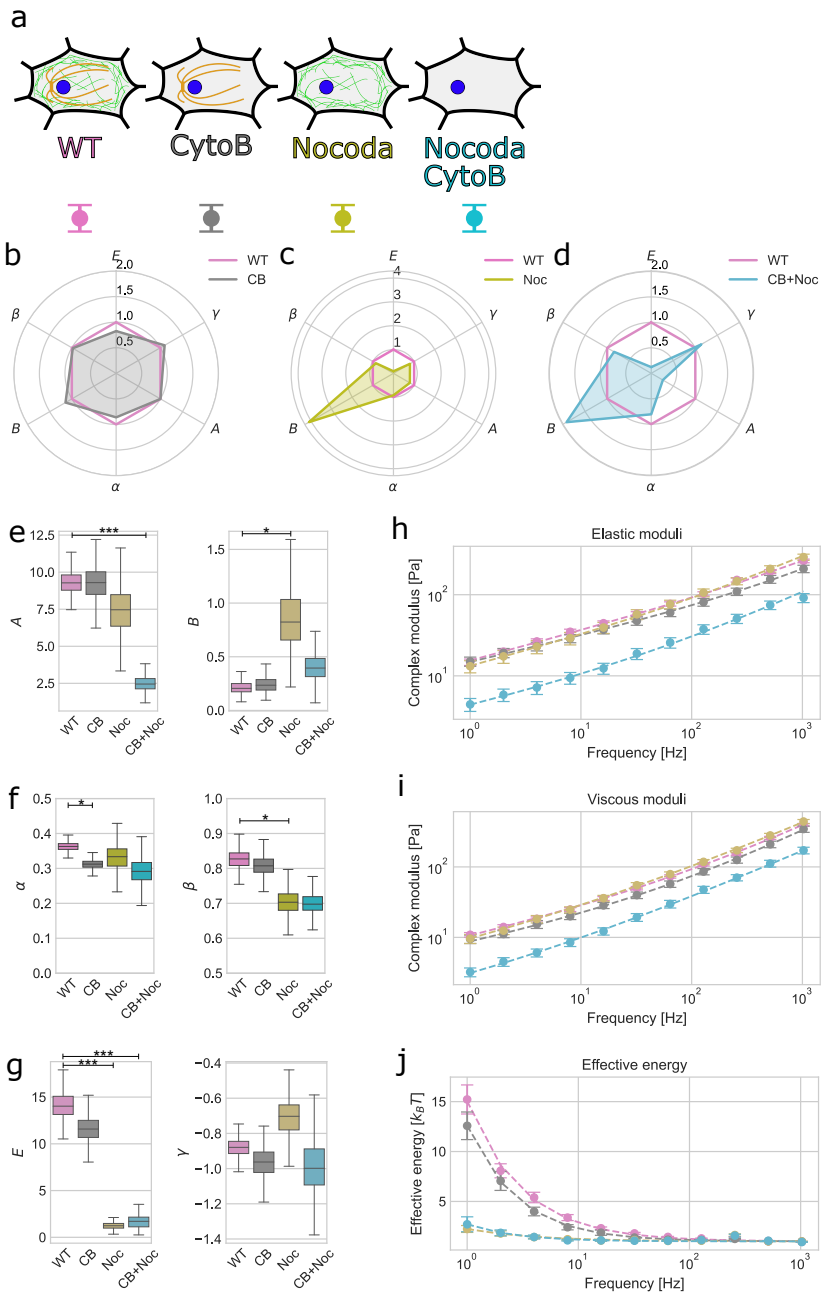

Figure 2: Wild type HeLa cells (WT) were treated with different cytoskeletal drugs to investigate their influence on the fingerprint parameters. a) Cytochalasin B (CytoB/CB) inhibits actin polymerization, Nocodazole (Nocoda/Noc) disturbs microtubule assembly and the combined treatment was used to disturb actin and microtubules simultaneously. b) The treatment with CB does not show a strong effect on the fingerprint parameters. c) Using Noc, intracellular activity in terms of E is strongly decreased while also the parameter B increases. d) The combined treatment shows a strong effect in decreasing intracellular activity E but also drastically softens the cytoplasm which is reflected in a decreased factor A. e,f,g) Change of fingerprint parameters in response to drug treatment. h,i,j) Effect of pharmacological treatment shown for the elastic modulus, loss modulus and effective energy

of MT did not reduce the contribution of the solid-like material properties A significantly. This result suggests that a yet unknown control mechanism stabilizes the intracellular mechanical properties of the solid-like material contribution. Cross-talk and feedback-loops between cytoskeletal structures are well known.[38] A possible mechanism could be the known up-regulation of actin polymerization upon MT depolymerization.[39,40] If the stability of the prefactor A, the solid-like contribution, is due to a compensation mechanism where actin compensates MT, a double disruption should have a drastic effect, as any in-built compensation is suppressed. Indeed, when disrupting the actin and the MT network simultaneously, we do find the expected drop in both the active forces driving particle fluctuations, and the contribution of the solid-like material marked by a collapse of the prefactor A (Figure 2d,e,g blue).

Additionally, both treatments with Nocodazole are also accompanied by a significant increase in liquid-like prefactor B which indicates a yet not understood change in the cytoplasmic structure. Since the prefactor A is in general almost a magnitude larger than B, the overall viscoelastic properties are mainly dominated by A.

These results demonstrate not only that the mechanical fingerprint can be used to dissect the effect of cytoskeletal drugs on different properties but also the combined information obtained is a first hint that cells may use compensation mechanisms to regulate their intracellular mechanics.

Separating cell types by their mechanical fingerprint

As we have shown that these drastic pharmacological treatments largely affect the prefactor A of the solid-like material and the strength of the effective energy E driving intracellular fluctuations, we asked if these are indeed tuned by the cell to support certain biological functions. To test this idea, we decided to compare HeLa cells to two other cell types that have drastically different mechanical requirements according to their function. First, we hypothesized that a muscle cell needs to have an increased intracellular mechanical stiffness for its function as mechanical force generator. This suggests that muscle cells will be tuned to differ in the solid-like material properties with higher prefactor A.

As seen in Figure 3b, this is exactly what we found when comparing the cervical cancer HeLa cells with a murine derived myoblast cell line (C2C12). The solid-like material stiffness as quantified by A almost doubled, indicating a strong increase in intracellular resistance. Additionally the solid-like material exponent further decreased emphasising a more solid-like material (Figure 3b,d). All other fingerprint parameters did not change significantly.

Next we hypothesized that a fast-moving cell type would have increased active forces in the cytoplasm, and render it more liquid-like to be able to move quicker through the extra-cellular space. This hypothesis was tested using an immune cell model. Macrophages were obtained from a hematopoietic progenitor cell line that expresses HoxB8 under an estrogen promotor.[11,13] Upon removal of estrogen the cells differentiate within 3 days to macrophages that we term HoxB8 cells in the following for convenience. Again, our experimental analysis of the mechanical fingerprint perfectly confirmed the prediction based on the biological function of macrophages (Figure 3c). Firstly, the effective energy prefactor E more than doubled indicating an increased intracellular activity. Secondly, there are changes in most

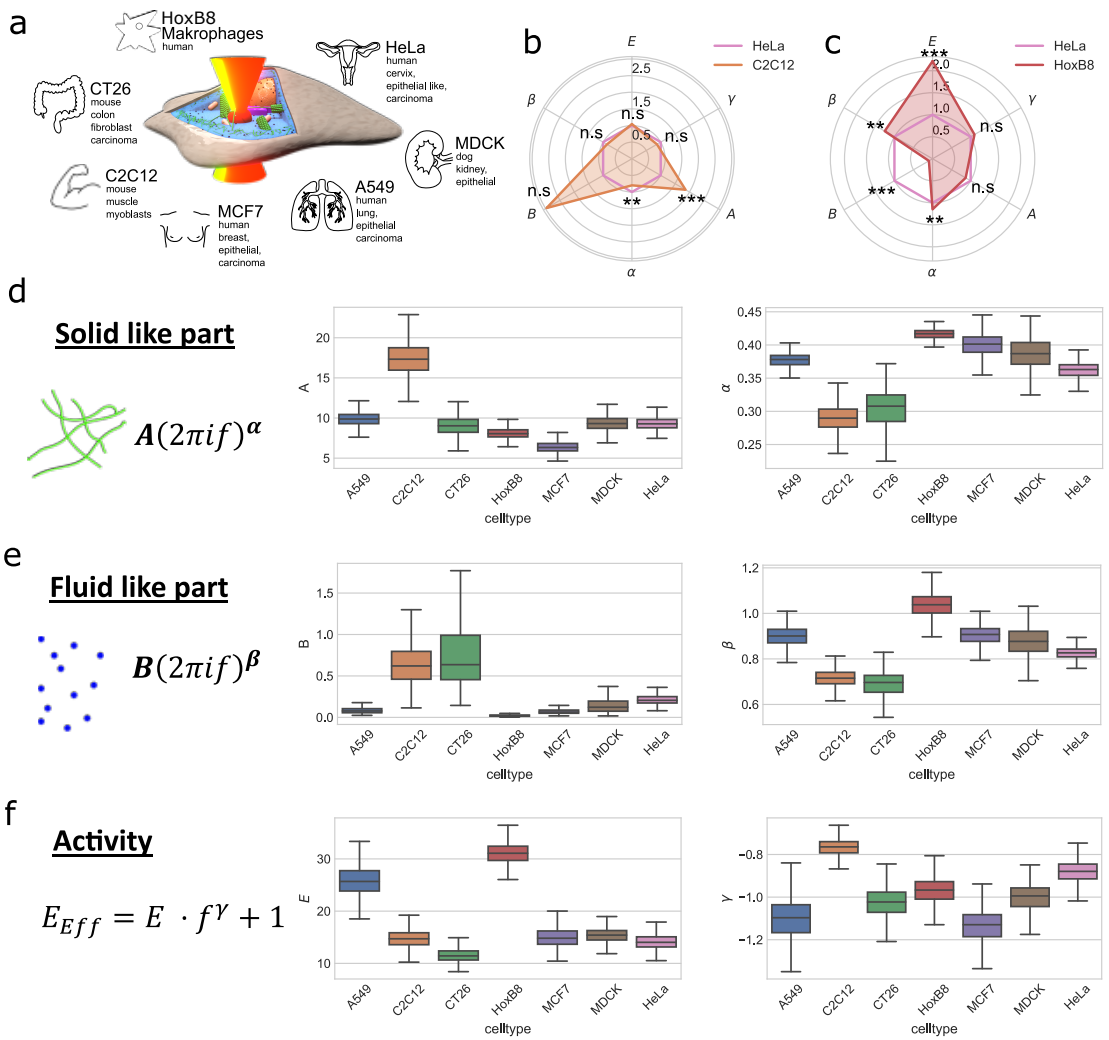

Figure 3: a) The mechanical fingerprint of 7 different cell types was determined by measuring their complex shear modulus and effective energy. b) Comparing HeLa cells to C2C12 muscle cells shows that muscle cells are overall stiffer (higher A). c) The comparison between HeLa cells and macrophages shows that macrophages of a higher intracellular activity (increased E) but are also more liquid- like and softer (increased α, β and decreased B) d-f). Using the fingerprint, active mechanical difference between cell types can be compared according to changes in the more solid-like material properties, more liquid-like material properties and the intracellular activity.

parameters describing the mechanical properties. Both exponents α and β are significantly increased. Strikingly, the viscosity defining prefactor B of the liquid-like material property collapsed indicating that the viscoelastic properties can quickly dissipate any large scale deformation of the whole cell. This suggests that both solid- and fluid-like material components are tuned towards more liquid-like materials with a lower viscous component. Our result is in perfect agreement with measurements obtained previously on the whole cell level.[41]

These results furthermore support the hypothesis that cells are able to adjust their mechanical fingerprint depending on their biological function. Muscle cells, requiring higher mechanical resistance, show a large solid-like prefactor, while immune cells that need to migrate quickly and deform easily are more liquid-like with lower viscous dissipation and generate a larger cytoplasmic active energy.

The mechanical fingerprint is different across cell types and species

Motivated by the finding that different cell types have different mechanical properties as quantified by the mechanical fingerprint, we wondered whether this approach can be used as a strategy to differentiate between cell types in terms of mechanical properties. In detail, we ask if at least one of the 6 parameters of the mechanical fingerprint are statistically different when comparing different cell types. Hence, we decided to determine the 6 parameter fingerprint for 7 different cell types (Figure 3a), of various function and from various species. In addition to the already introduced human HeLa, murine C2C12 and HoxB8 cells, we measured the fingerprint of human lung epithelial cells (A549), a murine fibroblast-like colon carcinoma cell line (CT26), a canine kidney epithelial cell line (MDCK) and a non-invasive human breast cancer cell line (MCF7). Figure 3d-f shows the variations of the 6 fingerprint parameters across all seven cell types.

In a first analysis, we looked at all possible pair-wise combinations of cells to test our hypothesis that the 6 parameters are sufficient to differentiate between cell types. Indeed, in most of the 21 possible combinations we found at least one of the fingerprint parameters to be different (Figure 4a, SI 2.2). Interestingly, the combinations of cell types where no significantly different parameter could be found are epithelial cells MDCK, HeLa and MCF7 as well as the fibroblast CT26. On average 2.1 parameters showed a significant difference. However, this analysis does not take into account the extent of significant difference. To approach this question more systematically, we use a variant of the z-score, where we normalize the difference in the mean values by twice the geometric average of the standard deviation the bootstrapped data. The z-score hence quantifies the extend of deviation between cells that is carried by a single parameter. For example the z-score of A between HeLa and CT26 is:

$$z^{A}_{HeLa,CT26} = \frac{< A_{HeLa} > - < A_{CT26} >}{2\sqrt{\sigma^2_{A,HeLa} + \sigma^2_{A,CT26}}} \tag{5}$$

Here, any value larger than 1 can be considered to mark a significant difference, and the larger the z-score the better the two cells can be separated according to the respective parameter. We then calculated the z-score for all 6 fingerprint

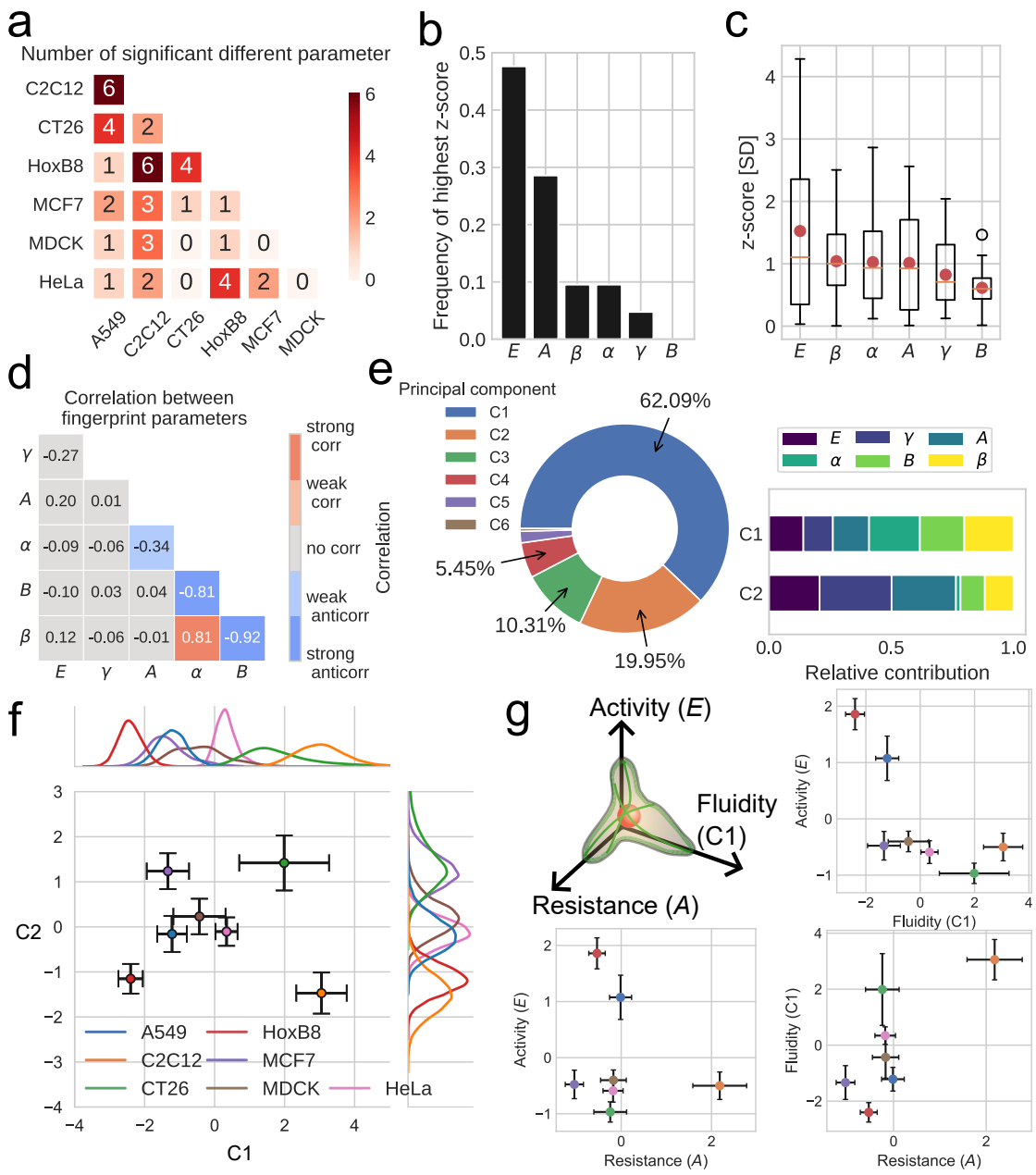

Figure 4: a) Number of significant different fingerprint parameter in pairwise cell type comparisons. b) Frequency of parameters showing the highest z-score. c) Distribution of z-score for all parameters for pairwise cell comparison. d) Correlation analysis between fingerprint parameters shows that not all parameters are varied independently. e) left: Explained variance ratio of the different principal components. Almost 80% of the variance is explained using the first two components. right: Relative contribution of the fingerprint parameter to the first two principal components. C1 mainly consists of α, β and B, C2 mainly consists of A, E, γ. f) Plotting all cell types according tothe first two principal components C1 and C2 shows that two parameters are already sufficient to distinguish between most cell types. g) Qualitative phase diagram of the active mechanical space. Activity, mainly captured by parameter E_0, resistance, dominated by A and solid-liquid switching can be described as fluidity that is determined by principal component 1 (C1) are varied among different cell types. Using this three dimensional space allows to identify physical differences among different cell types which may be related to function.

parameters across all 21 different pairs of cells. It should be noted that, in contrast to the p-value of the t-test, this values depends only on the first moments of the probability distributions, and is independent of the number of samples. Hence it reflects the average properties of each cell type, rather than a statistical measure. In a first step we studied which of the parameters was best to differentiate between the cells. Figure 4b shows how often each parameter was the best discriminator. We see that E and A are the most important parameters to distinguish between different cell types as they together show the highest z-score in more than almost 80% of the cases. As they mainly characterize the solid-like material properties and overall activity, this result implies that these properties are highly dependent on cell type and function. Additionally, we directly plot the z-scores of all cell pairs for the different parameters (Figure 4c). In contrast to the previous quantity, here the value of the z-scores becomes important. Despite E and A having most frequently the highest z-score, we also observed that the average z-score for the parameters β, α, A, γ and B was similar or smaller than 1, suggesting that the combination of all 6 parameters is relevant for characterizing the mechanical state of cells. The similarity in average z-scores may also indicate that there are correlations between these parameters, which could be due to underlying biological mechanisms.

To further explore this possibility we look at the correlation values (c.v.) (M 3.4) between the fingerprint parameters across all measurements as depicted in Figure 4de. We define an absolute c.v. below 0.3 as no (anti)correlation, between 0.3 and 0.6 as weak (anti)correlation and above 0.6 as strong (anti)correlation. While for most parameter pairs no correlation is observed, we find a strong dependency between parameters B, β and α and a weak anticorrelation between A and α. While α and β are positively correlated (0.81), both are negatively correlated with B (-0.81 and -0.92). Notably, the changes already observed for the more fluid-like HoxB8 cells do perfectly follow these correlations. A simultaneous variation of α, β and B might be a way for the cell to switch between a solid- and fluid-like state. This finding also implies that, even though the two power law approach is able to perfectly describe the observed viscoelastic properties, it might over-fit the data as some parameters are not fully independent. The cytoplasm does not seem to consist of two independent classes of materials but instead a deeper underlying mechanism might regulate the low-frequency elastic-like behaviour just as the high frequency more fluid-like behaviour.

In order to see if we can indeed further reduce the number of parameters required to describe the active intracellular mechanical state we performed a principal component analysis (PCA) (M 3.5). The explained variance ratio of each component is presented in Figure 4e left. Already 92% percent of the variance can be explained using only the first 3 components and 81% can even be explained with just 2 components. This supports the hypothesis that few underlying biological mechanisms act as "hyper parameters", which tune the mechanical fingerprint of the intracellular space.

Each principal component is a superposition of the normalized fingerprint parameters. We therefore wondered which fingerprint parameters dominate the first 2 principal components. Looking at the relative contributions (Figure 4e right , SI 2.1), we find that the first component C1, that explains 62.09% of all variance in data, mainly consists of fingerprint parameters α, B and β (21%, 18%, 20%). Finding these parameters combined in a single principal component is expected

as they also show strong correlation (Figure 4e) but strikingly, even though neither parameter by itself appeared to be dominant in characterizing the intracellular state in the previous analysis (Figure 4b,c), the combined component C1 seems to be the most relevant principal component. The second component C2 consists of the remaining fingerprint parameter E, γ and A (20%, 29%, 27%).

To determine whether C1 and C2 are already sufficient to distinguish between cell types, we plot the cell types according to these two parameters (Figure 4f). We observe that most cell types appear to separate from one another, indicating that C1 and C2 are effective in distinguishing between them. Interestingly, there are some cell types (HeLa, MDCK, A549) that cluster together, suggesting that they share similar mechanical properties. Whether this clustering is related to the fact that all these cells are of epithelial origin remains to be studied in more detail in future work.

As the first 2 components are sufficient to differentiate between most different cell types we wondered if they can be mapped on a physical interpretation. The first component C1 consists mainly of the parameters α, β and B. Additionally to the high correlation between the parameters, the increase of C1 represents an effective switch from a more solid material towards a fluid material, which we interpret hence as a parameter marking the fluidity of the cell. In contrast, the second component is largely a combination is solid-like material prefactor A and the intracellular activity parameter E. Hence, increasing C2 may either be interpreted as cellular stiffening or increase in mechanical activity. To avoid this ambiguity, while conserving the key features of the principle component analysis we propose a qualitative three dimensional phase space which consists of activity (mainly E) cellular resistance (mainly A) and fluidity (principal component C1)(Figure 4g). Although in principle both, A and B contribute to the mechanical resistance of a material when moving thought it, our finding that A is always much larger than B motivates to identify A with a mechanical resistance. Observation of the different cell types in this face space allows to identify key functional differences (Figure 4 g). Although HoxB8 macrophages and cancerous A549 cells display the highest activity, they together with MCF7 cells show the most fluid like phase and the lowest resistance. Speculatively, a high activity paired with a decreased resistance and higher fluidity might be advantageous for both motile cancer but also immune cells. On the other hand C2C12 muscle cells show the highest resistance paired with the most solid like phase, underlying that these cells might have fundamentally different active mechanical properties then other cell types with different function. As already seen in the PCA, epithelial cell types HeLa, MDCK and MCF7 show overall more similar properties with the largest differences observed along the fluid-solid like phase.

Conclusion

The here introduced mechanical fingerprint now opens the way for a systematic and functional study and characterization of the intracellular mechanical properties. The finding that HeLa cells can largely compensate for the mechanical loss of support upon microtubule polymerization suggests a functional role for the know up-regulation of actin polymerization upon MT depolymerization. This notion that the mechanical fingerprint is tuned to the cellular function is further

supported by the expected mechanical properties when extending the comparison to muscle and immune cells, where the increase in stiffness of muscle and decrease in viscosity on immune cells does perfectly fit their biological function. A key mechanical switch is a change between solid to fluid characteristics, which is directly reflected in a superposition of the fingerprint parameters that carries the most separating potential. This first principal component can be identified with a fluidity and completes the three dimensional phase space that we propose to use for placing cells in a functional relation to their mechanical fingerprint.

Material and Methods

M 1 Optical setup

In this study we use an optical tweezers setup that has been previously described[34] to perform active and passive microrheology measurements and apply well defined forces onto phagocytozed probe particles in living cells. Briefly, the setup is based on a home-build bright field microscope equipped with an 60x NA 1.2 Objective, where we employ two different lasers. A 808 nm laser (LU0808M250, 808 nm, 250 mW Lumics GmbH, Berlin,331Germany) is operated at moderate power (70 mW at sample plane) to allow for stable optical trapping and force application to probe particles at the focal plane. The lateral position of this laser can be precisely controlled with a piezo-based tilting mirror. Using a high NA=1.4 condenser, most of the transmitted laser light is collected. By projecting the back focal plane of the condenser onto a position sensitive detector (PSD), the trapping forces can be directly quantified.[42] A second, stationary, laser (L976- PAG500, 976 nm, 500 mW, Thorlabs, New Jersey, USA) is operated at low laser power (1 mW at sample plane) to not apply any relevant trapping forces. This laser is utilized to monitor the bead displacement via back focal plane interferometry[43] with nm precision. A schematic of this setup is depicted in Figure 1a.

M 2 Active and passive microrheology in cells

In order to conduct active and passive microrheology measurements, we utilized the previously desribed optical tweezers setup (see Figure 1a). Cells were prepared following the protocols outlined in Materials and Methods M 4. Throughout the experiments, the cells were maintained at 37 °C and 5% CO2 to ensure physiological conditions. We investigated a minimum of N=60 cells for each cell type or condition over the course of n=3 consecutive days. Data points were recorded at a sampling rate of 65 536 Hz.

M 2.1 Active microrheology

In active microrheology, the 808 nm trapping laser is employed to oscillate with a variable driving frequency f_D, exerting a sinusoidal force $F(t)$ onto a probe particle located inside a cell. Simultaneously, a second position detection laser records the position $x(t)$ of the particle. The relationship between the particle's position and the applied force is determined by the response function $\chi(t)$, as given by:

$$x(t) = \int_{-\infty}^{t} \chi(t - t')F(t')\mathrm{d}t'. \tag{6}$$

In the frequency domain, this convolution can be evaluated as a product, providing access to the response function:

$$\chi(f) = \frac{\tilde{x}(f)}{\tilde{F}(f)}, \tag{7}$$

which characterizes the viscoelastic properties of the probed region. Here, $\tilde{x}$ and $\tilde{F}$ denote the Fourier transform of position and force.

To obtain the frequency-dependent response function, the probe particle is successively driven at different driving frequencies ($f_D \in$ 1Hz, 2Hz, 4Hz, 8Hz, 16Hz, 32Hz, 64Hz, 128Hz, 256Hz, 512Hz, 1024Hz). At each frequency, a minimum of 3 periods were recorded, with a maximum duration of 1 second. Utilizing the generalized Stokes-Einstein relation:[44]

$$G^*(f) = \frac{1}{6\pi R\chi(f)}, \tag{8}$$

where R represents the particle radius, we determine the complex shear modulus $G^*(f)$.

Passive microrheology

In passive micro rheology measurements, free particle fluctuations inside the cells are recorded without application of external forces. In this study we employ the weak detection laser and back focal plane interferometry to track the bead displacement with high spatial and temporal precision. The particle position $x(t)$ is tracked 3 consecutive times over a time span of 10 s for each cell investigated. For each time series $x(t)$, we calculate the power spectral density (PSD)

$$\tilde{C}(f) = |\tilde{x}(f)|^2 \tag{9}$$

and average it over the 3 repetitions.

In equilibrium systems, the PSD is linked to the mechanical properties of the system via a generalized fluctuation-dissipation theorem (FDT):[44,45]

$$\tilde{C}(f) = \frac{k_\mathrm{B}T\chi''(f)}{\pi f} \tag{10}$$

Here k_BT is the thermal energy of the system and $\chi''(f)$ the imaginary part of the response function. In passive systems, this equation is valid and $\tilde{C}(f)$ can be used to determine the mechanical properties of the system. Living cells, however, are non-equilibrium systems. Metabolic energy leads to stronger particle fluctuations $\tilde{C}(f)$ than one would expect for a passive systems. We define an effective energy by adding an active cellular energy E_{active} to the thermal energy:

$$E_\mathrm{Eff}(f) = E_{active}(f) + k_\mathrm{B}T \tag{11}$$

This is the energy required to explain the particle fluctuations $\tilde{C}(f)$ given the mechanical properties $\chi''(f)$ measured in active microrheology. This yields a new adapted version of the FDT:

$$\tilde{C}(f) = \frac{E_{\mathrm{Eff}}(f)\chi''(f)}{\pi f} \tag{12}$$

By separately measuring $\chi''(f)$ in active microrheology and $\tilde{C}(f)$ in passive microrhelogy, we gain access to the effective energy of the system and thereby the level of non-equilibrium:

$$E_{\mathrm{Eff}}(f) = \frac{C(f)}{\chi''(f)} \frac{\pi f}{k_{\mathrm{B}}T} \tag{13}$$

The effective energy quantifies the level of activity in the system. Any deviation from 1 is indicative for non-equilibrium.

M 3 Statistical analysis

M 3.1 Bootstrapping

Bootstrapping is employed to get an estimate for the distribution of the mean cellular active mechanical properties. The following scheme is used:

- We have i experimental conditions, either different cell-types or drug treatments. For each condition i, we investigate N_i different cells. For each cell, we obtain curves for G',G'' and E_{Eff}
- For each condition i, the bootstrapping data set is generated. N_i samples are drawn with replacement with consecutive mean calculations. This process is repeated $N_{\mathrm{bootstrap}}$=10.000 times for each quantity of interest.
- The resulting distribution of curves captures the distribution of the means.
- Each curve is subsequently fit with the respective model which in turn also yields the distribution of the mean fit parameters.

M 3.2 Significance tests

Statistical tests between parameters obtained by the bootstrapping scheme (M 3.1) are conducted in the following way, a visualization of this process is depicted in SI Figure 1.

- We subtract the individual parameter distributions from each other. With this new distribution, we can check if 0 falls outside of the confidence interval.
- We agree on confidence intervals for significance $\alpha = 0.05$ for *, $\alpha = 0.01$ for ** and $\alpha = 0.001$ for ***.
- Next we do a Bonferroni correction: $\alpha_{corr} = \alpha/i$ with i being the number of experimental conditions.

- If 0 is outside the interval $[\alpha_{corr} : 1 - \alpha_{corr}]$, then the significance level is reached

M 3.3 Z-score

We use an adapted z-score to quantify how different a certain parameter is between two different cell types.

$$z = \frac{< A_{HeLa} > - < A_{CT26} >}{2\sqrt{\sigma^2_{A,HeLa} + \sigma^2_{A,CT26}}} \tag{14}$$

Here σ is the standard deviation SD.

M 3.4 Correlation analysis

Correlation analysis was performed using the corrcoef function of the python package numpy.[46]

M 3.5 Principal component analysis PCA

In order to see if the complexity of the 6 parameter fingerprint $E_0, E_1, A, \alpha, B, \beta$ can be further reduced, we performed a principal component analysis on the data. To this end, we utilized the function `sklearn.decomposition.PCA` from the Python module skicit learn.[47]The data was normalized prior to the pca using the `sklearn.preprocessing.StandardScaler` method.

M 4 Cell culture and bead insertion

A549, C2C12, CT26, HeLa, and MDCK cells were cultured in Dulbecco's modified Eagle medium (DMEM, Capricorn) supplemented with 1% Penicillin Streptomycin (Gibco) and 10% fetal bovine serum (FBS, Sigma-Aldrich) at a temperature of 37°C and 5% CO_2.

HoxB8 cells, provided by the Institute for Immunology at the University of Münster, Germany, were cultured according to a protocol described elsewhere.[11] To induce differentiation into macrophages, HoxB8 cells were suspended in differentiation medium three days prior to the experiment. After this, the same procedure as for the other cell lines, with the exception of using EDTA instead of Trypsin, was applied.

Cells were split when they reached near full confluency and seeded onto Fibronectin-coated glass cover slips (22x55x0.15 mm VWR). Medium was then aspirated, and a fresh 1:10,000 dilution of 1 µm beads (Polybead® Microspheres 1 µm, Polyscience, Inc) in medium was added to the sample . Cells where incubated for up to 15 hours to allow for adequate bead phagocytosis. Then, cells were washed with PBS to remove any residual extracellular beads. Following aspiration of PBS, a cover slip was fixed to the estimated cell spreading area using two layers of 200 µm adhesive tape (DST1950, Thorlabs, New Jersey, USA).

The sample chamber was filled with CO_2-independent medium (CO_2 Independent Medium, Gibco™) to ensure optimal cell viability during the experiments.

M 5 Pharmacological treatment

Cytochalasin B (Sigma-Aldrich), used for depolymerization of actin filaments, and Nocodazole (Sigma-Aldrich), employed for microtubule depolymerization, were employed in this study. Both drugs were applied at a concentration of $10\,\mu g\,mL^{-1}$ by adding them to the medium 10 minutes prior to the experiment.

References

[1] C.-P. Heisenberg and Y. Bellaïche, "Forces in tissue morphogenesis and patterning," Cell, vol. 153, pp. 948–962, May 2013.

[2] L. G. Pimpale, T. C. Middelkoop, A. Mietke, and S. W. Grill, "Cell lineage-dependent chiral actomyosin flows drive cellular rearrangements in early caenorhabditis elegans development," eLife, vol. 9, July 2020.

[3] G. G. Gundersen and H. J. Worman, "Nuclear positioning," Cell, vol. 152, pp. 1376–1389, Mar. 2013.

[4] S. A. Ruiz and C. S. Chen, "Emergence of patterned stem cell differentiation within multicellular structures," Stem Cells, vol. 26, pp. 2921–2927, Nov. 2008.

[5] D. T. Tambe, C. C. Hardin, T. E. Angelini, K. Rajendran, C. Y. Park, X. Serra-Picamal, E. H. Zhou, M. H. Zaman, J. P. Butler, D. A. Weitz, J. J. Fredberg, and X. Trepat, "Collective cell guidance by cooperative intercellular forces," Nat. Mater., vol. 10, pp. 469–475, June 2011.

[6] A. D. Doyle, F. W. Wang, K. Matsumoto, and K. M. Yamada, "One-dimensional topography underlies three-dimensional fibrillar cell migration," Journal of Cell Biology, vol. 184, pp. 481–490, Feb 2009.

[7] A. Pitaval, Q. Tseng, M. Bornens, and M. Théry, "Cell shape and contractility regulate ciliogenesis in cell cycle-arrested cells," J. Cell Biol., vol. 191, pp. 303–312, Oct. 2010.

[8] G. Fläschner, C. I. Roman, N. Strohmeyer, D. Martinez-Martin, and D. J. Müller, "Rheology of rounded mammalian cells over continuous high-frequencies," Nature Communications, vol. 12, p. 2922, May 2021.

[9] M. Li, D. Dang, L. Liu, N. Xi, and Y. Wang, "Atomic force microscopy in characterizing cell mechanics for biomedical applications: A review," IEEE Transactions on NanoBioscience, vol. 16, pp. 523–540, Sept. 2017.

[10] E. Evans and A. Yeung, "Apparent viscosity and cortical tension of blood granulocytes determined by micropipet aspiration," Biophysical Journal, vol. 56, pp. 151–160, July 1989.

[11] H. Schürmann, F. Abbasi, A. Russo, A. D. Hofemeier, M. Brandt, J. Roth, T. Vogl, and T. Betz, "Analysis of monocyte cell tractions in 2.5d reveals mesoscale mechanics of podosomes during substrate-indenting cell protrusion," Journal of Cell Science, vol. 135, p. jcs259042, May 2022.

[12] H. D. Belly, A. Stubb, A. Yanagida, C. Labouesse, P. H. Jones, E. K. Paluch, and K. J. Chalut, "Membrane tension gates ERK-mediated regulation of pluripotent cell fate," Cell Stem Cell, vol. 28, pp. 273–284.e6, Feb. 2021.

[13] N. Wang, I. M. Tolić-Nørrelykke, J. Chen, S. M. Mijailovich, J. P. Butler, J. J. Fredberg, and D. Stamenović, "Cell prestress. i. stiffness and prestress are closely associated in adherent contractile cells," American Journal of Physiology-Cell Physiology, vol. 282, pp. C606–C616, Mar 2002.

[14] P. Rosendahl, K. Plak, A. Jacobi, M. Kraeter, N. Toepfner, O. Otto, C. Herold, M. Winzi, M. Herbig, Y. Ge, S. Girardo, K. Wagner, B. Baum, and J. Guck, "Real-time fluorescence and deformability cytometry," Nature Methods, vol. 15, pp. 355–358, May 2018.

[15] S. Mathieu and J.-B. Manneville, "Intracellular mechanics: connecting rheology and mechanotransduction," Current Opinion in Cell Biology, vol. 56, pp. 34–44, Feb. 2019.

[16] M. Guo, A. J. Ehrlicher, M. H. Jensen, M. Renz, J. R. Moore, R. D. Goldman, J. Lippincott-Schwartz, F. C. Mackintosh, and D. A. Weitz, "Probing the stochastic, motor-driven properties of the cytoplasm using force spectrum microscopy," Cell, vol. 158, pp. 822–832, Aug 2014.

[17] J. Xie, J. Najafi, R. L. Borgne, J.-M. Verbavatz, C. Durieu, J. Sallé, and N. Minc, "Contribution of cytoplasm viscoelastic properties to mitotic spindle positioning," Proceedings of the National Academy of Sciences, vol. 119, Feb. 2022.

[18] G. Volpe, O. M. Maragò, H. Rubinsztein-Dunlop, G. Pesce, A. B. Stilgoe, G. Volpe, G. Tkachenko, V. G. Truong, S. N. Chormaic, F. Kalantarifard, P. Elahi, M. Käll, A. Callegari, M. I. Marqués, A. A. R. Neves, W. L. Moreira, A. Fontes, C. L. Cesar, R. Saija, A. Saidi, P. Beck, J. S. Eismann, P. Banzer, T. F. D. Fernandes, F. Pedaci, W. P. Bowen, R. Vaippully, M. Lokesh, B. Roy, G. Thalhammer-Thurner, M. Ritsch-Marte, L. P. García, A. V. Arzola, I. P. Castillo, A. Argun, T. M. Muenker, B. E. Vos, T. Betz, I. Cristiani, P. Minzioni, P. J. Reece, F. Wang, D. McGloin, J. C. Ndukaife, R. Quidant, R. P. Roberts, C. Laplane, T. Volz, R. Gordon, D. Hanstorp, J. T. Marmolejo, G. D. Bruce, K. Dholakia, T. Li, O. Brzobohatý, S. H. Simpson, P. Zemánek, F. Ritort, Y. Roichman, V. Bobkova, R. Wittkowski, C. Denz, G. V. P. Kumar, A. Foti, M. G. Donato, P. G. Gucciardi, L. Gardini, G. Bianchi, A. V. Kashchuk, M. Capitanio, L. Paterson, P. H. Jones, K. Berg-Sørensen, Y. F. Barooji, L. B. Oddershede, P. Pouladian, D. Preece, C. B. Adiels, A. C. D. Luca, A. Magazzù, D. B. Ciriza, M. A. Iatì, and G. A. Swartzlander, "Roadmap for optical tweezers," Journal of Physics: Photonics, vol. 5, p. 022501, Apr. 2023.

[19] B. H. Blehm, A. Devine, J. R. Staunton, and K. Tanner, "In vivo tissue has non-linear rheological behavior distinct from 3d biomimetic hydrogels, as determined by AMOTIV microscopy," Biomaterials, vol. 83, pp. 66–78, Mar. 2016.

[20] S. Hurst, B. E. Vos, M. Brandt, and T. Betz, "Intracellular softening and increased viscoelastic fluidity during division," Nature Physics, vol. 17, pp. 1270–1276, Nov 2021.

[21] C. Battle, C. P. Broedersz, N. Fakhri, V. F. Geyer, J. Howard, C. F. Schmidt, and F. C. MacKintosh, "Broken detailed balance at mesoscopic scales in active biological systems," Science, vol. 352, pp. 604–607, Apr. 2016.

[22] F. S. Gnesotto, F. Mura, J. Gladrow, and C. P. Broedersz, "Broken detailed balance and non-equilibrium dynamics in living systems: a review," Reports on Progress in Physics, vol. 81, p. 066601, Apr. 2018.

[23] M. Yousafzai, V. Yadav, S. Amiri, Y. Errami, S. Amiri, and M. Murrell, "Active regulation of pressure and volume defines an energetic constraint on the size of cell aggregates," Physical Review Letters, vol. 128, Jan. 2022.

[24] X. Fang and J. Wang, "Nonequilibrium thermodynamics in cell biology: Extending equilibrium formalism to cover living systems," Annual Review of Biophysics, vol. 49, pp. 227–246, May 2020.

[25] H. Yamaguchi and J. Condeelis, "Regulation of the actin cytoskeleton in cancer cell migration and invasion," Biochimica et Biophysica Acta (BBA) - Molecular Cell Research, vol. 1773, pp. 642–652, May 2007.

[26] P. P. Provenzano and P. J. Keely, "Mechanical signaling through the cytoskeleton regulates cell proliferation by coordinated focal adhesion and rho GTPase signaling," Journal of Cell Science, vol. 124, pp. 1195–1205, Apr. 2011.

[27] M. T. Abreu-Blanco, J. J. Watts, J. M. Verboon, and S. M. Parkhurst, "Cytoskeleton responses in wound repair," Cellular and Molecular Life Sciences, vol. 69, pp. 2469–2483, Feb. 2012.

[28] A. S. Moore, S. M. Coscia, C. L. Simpson, F. E. Ortega, E. C. Wait, J. M. Heddleston, J. J. Nirschl, C. J. Obara, P. Guedes-Dias, C. A. Boecker, T.-L. Chew, J. A. Theriot, J. Lippincott-Schwartz, and E. L. F. Holzbaur, "Actin cables and comet tails organize mitochondrial networks in mitosis," Nature, vol. 591, pp. 659–664, Mar 2021.

[29] A. A. Jord, G. Letort, S. Chanet, F.-C. Tsai, C. Antoniewski, A. Eichmuller, C. D. Silva, J.-R. Huynh, N. S. Gov, R. Voituriez, M.-É. Terret, and M.-H. Verlhac, "Cytoplasmic forces functionally reorganize nuclear condensates in oocytes," Nature Communications, vol. 13, Aug. 2022.

[30] G. Guigas, C. Kalla, and M. Weiss, "Probing the nanoscale viscoelasticity of intracellular fluids in living cells," Biophysical Journal, vol. 93, pp. 316–323, July 2007.

[31] A. Bonfanti, J. L. Kaplan, G. Charras, and A. Kabla, "Fractional viscoelastic models for power-law materials," vol. 16, no. 26, pp. 6002–6020.

[32] A. Rigato, A. Miyagi, S. Scheuring, and F. Rico, "High-frequency microrheology reveals cytoskeleton dynamics in living cells," Nature Physics, vol. 13, pp. 771–775, Aug 2017.

[33] A. Nguyen, M. Brandt, T. M. Muenker, and T. Betz, "Multi-oscillation microrheology via acoustic force spectroscopy enables frequency-dependent measurements on endothelial cells at high-throughput," Lab on a Chip, vol. 21, no. 10, pp. 1929–1947, 2021.

[34] T. M. Muenker, G. Knotz, M. Krüger, and T. Betz, "Onsager regression characterizes living systems in passive measurements," May 2022.

[35] W. W. Ahmed, É. Fodor, and T. Betz, "Active cell mechanics: Measurement and theory," Biochimica et Biophysica Acta (BBA) - Molecular Cell Research, vol. 1853, pp. 3083–3094, Nov 2015.

[36] F. C. MacKintosh and C. F. Schmidt, "Active cellular materials," Current Opinion in Cell Biology, vol. 22, pp. 29–35, Feb 2010.

[37] W. Junge, "ATP synthase and other motor proteins," Proc. Natl. Acad. Sci. U. S. A., vol. 96, pp. 4735–4737, Apr. 1999.

[38] S. Seetharaman and S. Etienne-Manneville, "Cytoskeletal crosstalk in cell migration," Trends in Cell Biology, vol. 30, pp. 720–735, Sept. 2020.

[39] T. Enomoto, "Microtubule disruption induces the formation of actin stress fibers and focal adhesions in cultured cells: Possible involvement of the rho signal cascade.," Cell Structure and Function, vol. 21, no. 5, pp. 317–326, 1996.

[40] A. Rape, W. hui Guo, and Y. li Wang, "Microtubule depolymerization induces traction force increase through two distinct pathways," Journal of Cell Science, vol. 124, pp. 4233–4240, Dec. 2011.

[41] A. E. Ekpenyong, G. Whyte, K. Chalut, S. Pagliara, F. Lautenschläger, C. Fiddler, S. Paschke, U. F. Keyser, E. R. Chilvers, and J. Guck, "Viscoelastic properties of differentiating blood cells are fate- and function-dependent," PLOS ONE, vol. 7, pp. 1–10, 09 2012.

[42] A. Farré and M. Montes-Usategui, "A force detection technique for single-beam optical traps based on direct measurement of light momentum changes," vol. 18, no. 11, pp. 11955–11968. Publisher: Optical Society of America.

[43] F. Marsà, A. Farré, E. Martín-Badosa, and M. Montes-Usategui, "Holographic optical tweezers combined with back-focal-plane displacement detection," Opt. Express, vol. 21, pp. 30282–30294, Dec 2013.

[44] T. G. Mason and D. A. Weitz, "Optical Measurements of Frequency-Dependent Linear Viscoelastic Moduli of Complex Fluids," Physical Review Letters, vol. 74, pp. 1250–1253, Feb. 1995. Publisher: American Physical Society.

[45] F. Gittes, B. Schnurr, P. D. Olmsted, F. C. MacKintosh, and C. F. Schmidt, "Microscopic viscoelasticity: Shear moduli of soft materials determined from thermal fluctuations," Phys. Rev. Lett., vol. 79, pp. 3286–3289, Oct 1997.

[46] C. R. Harris, K. J. Millman, S. J. van der Walt, R. Gommers, P. Virtanen, D. Cournapeau, E. Wieser, J. Taylor, S. Berg, N. J. Smith, R. Kern, M. Picus, S. Hoyer, M. H. van Kerkwijk, M. Brett, A. Haldane, J. F. del Río, M. Wiebe, P. Peterson, P. Gérard-Marchant, K. Sheppard, T. Reddy, W. Weckesser, H. Abbasi, C. Gohlke, and T. E. Oliphant, "Array programming with NumPy," Nature, vol. 585, pp. 357–362, Sept. 2020.

[47] F. Pedregosa, G. Varoquaux, A. Gramfort, V. Michel, B. Thirion, O. Grisel, M. Blondel, P. Prettenhofer, R. Weiss, V. Dubourg, J. Vanderplas, A. Passos, D. Cournapeau, M. Brucher, M. Perrot, and E. Duchesnay, "Scikit-learn: Machine learning in Python," Journal of Machine Learning Research, vol. 12, pp. 2825–2830, 2011.

Acknowledgements

We thank the Institute for Immunology from the University of Münster for providing us with HoxB8 cells and the corresponding resources. T.M.M., B.E.V. and T.B. have received funding from the European Research Council (ERC) under the European Union's Horizon 2020 research and innovation program (PolarizeMe, Grant agreement No. 771201). T.M.M., B.E.V. and T.B. have received funding from the DFG (Project number 516046415).

Author information

Affiliations

Third Institute of Physics, Georg August Universität Göttingen, Göttingen, Germany

Till M. Muenker, Timo Betz, B. E. Vos

Contributions

T.M.M. conceived and built the experimental setup, performed the experiments, performed the data analysis, interpreted the results and wrote the manuscript.

B.E.V. built the experimental setup, interpreted the results and wrote the manuscript.

T.B. conceived the study, interpreted the results and wrote the manuscript.

All authors discussed the results and commented on the manuscript.

Corresponding authors

Correspondence to

Till Münker: till.muenker@phys.uni-goettingen.de

Timo Betz: timo.betz@phys.uni-goettingen.de

Ethics declaration

Competing interests

No competing interests

Supplementary Information

SI 1 Supplementary Text

SI 1.1 Accounting for calibration error during active measurements

As explained in section M 1, the position of probe particles is determined using a weak detection laser and back focal plane interferometry. The voltage signal generated by a quadrant photo diode QDP corresponds to the particle position relative to the center of the laser. To get the correct proportionality constant between voltage signal and particle position, the setup was calibrated before each measurement. Therefore, the sample stage was moved by a known distance whilst recording the QPD signal. From this calibration curve the proportionality constant between QPD signal and particle position Ξ was calculated. This procedure allow for correct position detection during passive rheology experiments. For active measurements however, a second, stronger trapping laser was used. In addition to radial forces, this laser also exerts axial forces onto the particle, dragging it into the focal plane of the trapping laser. As this focal plane is not the exact plane in which Ξ was calibrated, active rheology experiments suffered from subtle errors in position detection.
To account for this error, we utilized the fact the motor proteins operate on a finite timescale and therefore do not attribute to intracellular activity on timescales larger than 500Hz.[37] Therefore, fluctuation dissipation theorem (FDT) has to be valid in such frequency regimes. We use this to scale the proportionality constant Ξ in active rheology experiments such that FDT is fulfilled in the mean between 512 Hz and 1024 Hz.

SI 2 Supplementary Tables

SI 2.1 Principal component analysis

		Principal axis in parameter space					
Component	Explained variance ratio	E_0	E_1	A	α	B	β
1	0.621	-0.338	0.290	0.356	-0.500	0.436	-0.484
2	0.199	-0.438	-0.624	-0.558	-0.039	0.210	-0.248
3	0.103	0.721	-0.420	0.094	-0.265	0.474	0.014
4	0.055	0.140	0.580	-0.647	0.053	0.454	0.129
5	0.018	-0.372	-0.120	0.327	0.267	0.525	0.627
6	0.004	-0.124	-0.014	-0.164	-0.777	-0.242	0.543

Table 1: Results of principal component analysis. Explained variance ratio quantifies how much information is captured by the corresponding component. The composition of each component is explained by its axis in parameter space. Here the values are shown until third decimal digit. Most information is explained by principal component 1 with an explained variance ration of 0.621. This component is mainly represented by fit parameter α, β and B in parameter space.

Table 2: Parameter E: different cell types

	A549	C2C12	CT26	HoxB8	MCF7	MDCK	HeLa
A549	p=1.0000(n.s.)	p=0.0001(***)	p=0.0000(***)	p=0.0554(n.s.)	p=0.0001(**)	p=0.0001(***)	p=0.0000(***)
C2C12	p=0.0001(***)	p=1.0000(n.s.)	p=0.0610(n.s.)	p=0.0000(***)	p=0.4822(n.s.)	p=0.3663(n.s.)	p=0.3929(n.s.)
CT26	p=0.0000(***)	p=0.0610(n.s.)	p=1.0000(n.s.)	p=0.0000(***)	p=0.0571(n.s.)	p=0.0143(n.s.)	p=0.0829(n.s.)
HoxB8	p=0.0554(n.s.)	p=0.0000(***)	p=0.0000(***)	p=1.0000(n.s.)	p=0.0000(***)	p=0.0000(***)	p=0.0000(***)
MCF7	p=0.0001(**)	p=0.4822(n.s.)	p=0.0571(n.s.)	p=0.0000(***)	p=1.0000(n.s.)	p=0.3975(n.s.)	p=0.3683(n.s.)
MDCK	p=0.0001(***)	p=0.3663(n.s.)	p=0.0143(n.s.)	p=0.0000(***)	p=0.3975(n.s.)	p=1.0000(n.s.)	p=0.2443(n.s.)
HeLa	p=0.0000(***)	p=0.3929(n.s.)	p=0.0829(n.s.)	p=0.0000(***)	p=0.3683(n.s.)	p=0.2443(n.s.)	p=1.0000(n.s.)

Table 3: Parameter γ: different cell types

	A549	C2C12	CT26	HoxB8	MCF7	MDCK	HeLa
A549	p=1.0000(n.s.)	p=0.0000(***)	p=0.2757(n.s.)	p=0.1303(n.s.)	p=0.3915(n.s.)	p=0.1996(n.s.)	p=0.0162(n.s.)
C2C12	p=0.0000(***)	p=1.0000(n.s.)	p=0.0006(**)	p=0.0017(*)	p=0.0000(***)	p=0.0005(**)	p=0.0405(n.s.)
CT26	p=0.2757(n.s.)	p=0.0006(**)	p=1.0000(n.s.)	p=0.2788(n.s.)	p=0.1573(n.s.)	p=0.4034(n.s.)	p=0.0476(n.s.)
HoxB8	p=0.1303(n.s.)	p=0.0017(*)	p=0.2788(n.s.)	p=1.0000(n.s.)	p=0.0486(n.s.)	p=0.3623(n.s.)	p=0.1365(n.s.)
MCF7	p=0.3915(n.s.)	p=0.0000(***)	p=0.1573(n.s.)	p=0.0486(n.s.)	p=1.0000(n.s.)	p=0.0979(n.s.)	p=0.0024(*)
MDCK	p=0.1996(n.s.)	p=0.0005(**)	p=0.4034(n.s.)	p=0.3623(n.s.)	p=0.0979(n.s.)	p=1.0000(n.s.)	p=0.0714(n.s.)
HeLa	p=0.0162(n.s.)	p=0.0405(n.s.)	p=0.0476(n.s.)	p=0.1365(n.s.)	p=0.0024(*)	p=0.0714(n.s.)	p=1.0000(n.s.)

Table 4: Parameter A: different cell types

	A549	C2C12	CT26	HoxB8	MCF7	MDCK	HeLa
A549	p=1.0000(n.s.)	p=0.0001(***)	p=0.2976(n.s.)	p=0.0441(n.s.)	p=0.0005(**)	p=0.3361(n.s.)	p=0.3107(n.s.)
C2C12	p=0.0001(***)	p=1.0000(n.s.)	p=0.0001(***)	p=0.0000(***)	p=0.0000(***)	p=0.0000(***)	p=0.0000(***)
CT26	p=0.2976(n.s.)	p=0.0001(***)	p=1.0000(n.s.)	p=0.2444(n.s.)	p=0.0236(n.s.)	p=0.4380(n.s.)	p=0.4344(n.s.)
HoxB8	p=0.0441(n.s.)	p=0.0000(***)	p=0.2444(n.s.)	p=1.0000(n.s.)	p=0.0340(n.s.)	p=0.1388(n.s.)	p=0.1060(n.s.)
MCF7	p=0.0005(**)	p=0.0000(***)	p=0.0236(n.s.)	p=0.0340(n.s.)	p=1.0000(n.s.)	p=0.0060(n.s.)	p=0.0023(*)
MDCK	p=0.3361(n.s.)	p=0.0000(***)	p=0.4380(n.s.)	p=0.1388(n.s.)	p=0.0060(n.s.)	p=1.0000(n.s.)	p=0.4971(n.s.)
HeLa	p=0.3107(n.s.)	p=0.0000(***)	p=0.4344(n.s.)	p=0.1060(n.s.)	p=0.0023(*)	p=0.4971(n.s.)	p=1.0000(n.s.)

Table 5: Parameter α: different cell types

	A549	C2C12	CT26	HoxB8	MCF7	MDCK	HeLa
A549	p=1.0000(n.s.)	p=0.0000(***)	p=0.0034(*)	p=0.0018(*)	p=0.1668(n.s.)	p=0.3630(n.s.)	p=0.1758(n.s.)
C2C12	p=0.0000(***)	p=1.0000(n.s.)	p=0.3298(n.s.)	p=0.0000(***)	p=0.0026(*)	p=0.0004(**)	p=0.0006(**)
CT26	p=0.0034(*)	p=0.3298(n.s.)	p=1.0000(n.s.)	p=0.0000(***)	p=0.0086(n.s.)	p=0.0098(n.s.)	p=0.0217(n.s.)
HoxB8	p=0.0018(*)	p=0.0000(***)	p=0.0000(***)	p=1.0000(n.s.)	p=0.1910(n.s.)	p=0.0992(n.s.)	p=0.0004(**)
MCF7	p=0.1668(n.s.)	p=0.0026(*)	p=0.0086(n.s.)	p=0.1910(n.s.)	p=1.0000(n.s.)	p=0.3362(n.s.)	p=0.0887(n.s.)
MDCK	p=0.3630(n.s.)	p=0.0004(**)	p=0.0098(n.s.)	p=0.0992(n.s.)	p=0.3362(n.s.)	p=1.0000(n.s.)	p=0.1878(n.s.)
HeLa	p=0.1758(n.s.)	p=0.0006(**)	p=0.0217(n.s.)	p=0.0004(**)	p=0.0887(n.s.)	p=0.1878(n.s.)	p=1.0000(n.s.)

Table 6: Parameter B: different cell types

	A549	C2C12	CT26	HoxB8	MCF7	MDCK	HeLa
A549	p=1.0000(n.s.)	p=0.0005(**)	p=0.0015(*)	p=0.0232(n.s.)	p=0.4187(n.s.)	p=0.2814(n.s.)	p=0.0381(n.s.)
C2C12	p=0.0005(**)	p=1.0000(n.s.)	p=0.4586(n.s.)	p=0.0000(***)	p=0.0045(n.s.)	p=0.0457(n.s.)	p=0.0165(n.s.)
CT26	p=0.0015(*)	p=0.4586(n.s.)	p=1.0000(n.s.)	p=0.0000(***)	p=0.0044(n.s.)	p=0.0483(n.s.)	p=0.0259(n.s.)
HoxB8	p=0.0232(n.s.)	p=0.0000(***)	p=0.0000(***)	p=1.0000(n.s.)	p=0.0338(n.s.)	p=0.0157(n.s.)	p=0.0000(***)
MCF7	p=0.4187(n.s.)	p=0.0045(n.s.)	p=0.0044(n.s.)	p=0.0338(n.s.)	p=1.0000(n.s.)	p=0.2474(n.s.)	p=0.0579(n.s.)
MDCK	p=0.2814(n.s.)	p=0.0457(n.s.)	p=0.0483(n.s.)	p=0.0157(n.s.)	p=0.2474(n.s.)	p=1.0000(n.s.)	p=0.2627(n.s.)
HeLa	p=0.0381(n.s.)	p=0.0165(n.s.)	p=0.0259(n.s.)	p=0.0000(***)	p=0.0579(n.s.)	p=0.2627(n.s.)	p=1.0000(n.s.)

Table 7: Parameter β: different cell types

	A549	C2C12	CT26	HoxB8	MCF7	MDCK	HeLa
A549	p=1.0000(n.s.)	p=0.0009(*)	p=0.0008(*)	p=0.0221(n.s.)	p=0.4734(n.s.)	p=0.3773(n.s.)	p=0.0818(n.s.)
C2C12	p=0.0009(*)	p=1.0000(n.s.)	p=0.3592(n.s.)	p=0.0000(***)	p=0.0061(n.s.)	p=0.0383(n.s.)	p=0.0091(n.s.)
CT26	p=0.0008(*)	p=0.3592(n.s.)	p=1.0000(n.s.)	p=0.0000(***)	p=0.0042(n.s.)	p=0.0269(n.s.)	p=0.0063(n.s.)
HoxB8	p=0.0221(n.s.)	p=0.0000(***)	p=0.0000(***)	p=1.0000(n.s.)	p=0.0252(n.s.)	p=0.0271(n.s.)	p=0.0002(**)
MCF7	p=0.4734(n.s.)	p=0.0061(n.s.)	p=0.0042(n.s.)	p=0.0252(n.s.)	p=1.0000(n.s.)	p=0.3654(n.s.)	p=0.1008(n.s.)
MDCK	p=0.3773(n.s.)	p=0.0383(n.s.)	p=0.0269(n.s.)	p=0.0271(n.s.)	p=0.3654(n.s.)	p=1.0000(n.s.)	p=0.2511(n.s.)
HeLa	p=0.0818(n.s.)	p=0.0091(n.s.)	p=0.0063(n.s.)	p=0.0002(**)	p=0.1008(n.s.)	p=0.2511(n.s.)	p=1.0000(n.s.)

SI 2.2 Significance tests after bootstrapping

Table 8: Parameter E: different drugs

	HeLa	CB	Noc	CB + Noc
HeLa	p=1.0000(n.s.)	p=0.1017(n.s.)	p=0.0000(***)	p=0.0000(***)
CB	p=0.1017(n.s.)	p=1.0000(n.s.)	p=0.0000(***)	p=0.0000(***)
Noc	p=0.0000(***)	p=0.0000(***)	p=1.0000(n.s.)	p=0.2946(n.s.)
CB + Noc	p=0.0000(***)	p=0.0000(***)	p=0.2946(n.s.)	p=1.0000(n.s.)

Table 9: Parameter γ: different drugs

	HeLa	CB	Noc	CB + Noc
HeLa	p=1.0000(n.s.)	p=0.2085(n.s.)	p=0.1167(n.s.)	p=0.2464(n.s.)
CB	p=0.2085(n.s.)	p=1.0000(n.s.)	p=0.0634(n.s.)	p=0.4286(n.s.)
Noc	p=0.1167(n.s.)	p=0.0634(n.s.)	p=1.0000(n.s.)	p=0.1114(n.s.)
CB + Noc	p=0.2464(n.s.)	p=0.4286(n.s.)	p=0.1114(n.s.)	p=1.0000(n.s.)

Table 10: Parameter A: different drugs

	HeLa	CB	Noc	CB + Noc
HeLa	p=1.0000(n.s.)	p=0.4718(n.s.)	p=0.1572(n.s.)	p=0.0000(***)
CB	p=0.4718(n.s.)	p=1.0000(n.s.)	p=0.1935(n.s.)	p=0.0000(***)
Noc	p=0.1572(n.s.)	p=0.1935(n.s.)	p=1.0000(n.s.)	p=0.0004(**)
CBC + Noc	p=0.0000(***)	p=0.0000(***)	p=0.0004(**)	p=1.0000(n.s.)

Table 11: Parameter α: different drugs

	HeLa	CB	Noc	CB + Noc
HeLa	p=1.0000(n.s.)	p=0.0025(*)	p=0.2016(n.s.)	p=0.0500(n.s.)
CB	p=0.0025(*)	p=1.0000(n.s.)	p=0.2976(n.s.)	p=0.3061(n.s.)
Noc	p=0.2016(n.s.)	p=0.2976(n.s.)	p=1.0000(n.s.)	p=0.2475(n.s.)
CB + Noc	p=0.0500(n.s.)	p=0.3061(n.s.)	p=0.2475(n.s.)	p=1.0000(n.s.)

Table 12: Parameter B: different drugs

	HeLa	CB	Noc	CB + Noc
HeLa	p=1.0000(n.s.)	p=0.3715(n.s.)	p=0.0031(*)	p=0.1159(n.s.)
CB	p=0.3715(n.s.)	p=1.0000(n.s.)	p=0.0066(n.s.)	p=0.1686(n.s.)
Noc	p=0.0031(*)	p=0.0066(n.s.)	p=1.0000(n.s.)	p=0.0636(n.s.)
CB + Noc	p=0.1159(n.s.)	p=0.1686(n.s.)	p=0.0636(n.s.)	p=1.0000(n.s.)

Table 13: Parameter β: different drugs

	HeLa	CB	Noc	CB + Noc
HeLa	p=1.0000(n.s.)	p=0.3164(n.s.)	p=0.0042(*)	p=0.0194(n.s.)
CB	p=0.3164(n.s.)	p=1.0000(n.s.)	p=0.0098(n.s.)	p=0.0295(n.s.)
Noc	p=0.0042(*)	p=0.0098(n.s.)	p=1.0000(n.s.)	p=0.4784(n.s.)
CB + Noc	p=0.0194(n.s.)	p=0.0295(n.s.)	p=0.4784(n.s.)	p=1.0000(n.s.)

SI 2.3 R^2-values for fits of bootstrapped data

Table 14: R^2-values fGKV fit of complex shear moduli - bootstrapped data

Celltype	R^2 $G'(f)$	R^2 $G''(f)$
A549	0.999	0.997
C2C12	0.998	0.998
CT26	0.997	0.998
HoxB8	0.999	0.993
MCF7	0.996	0.996
MDCK	0.997	0.999
HeLa	0.998	0.999
CytoB	0.998	0.999
Noc	0.999	0.999
CytoB + Noc	0.997	0.999

Table 15: R^2-values power law fit of effective energy - bootstrapped data

Celltype	$R^2 E_{\mathrm{Eff}}(f)$
A549	0.997
C2C12	0.997
CT26	0.993
HoxB8	0.993
MCF7	0.996
MDCK	0.994
HeLa	0.996
CytoB	0.998
Noc	0.798
CytoB + Noc	0.711

SI 2.4 R^2-values for fits of not bootstrapped data

Table 16: R^2-values fGKV fit of complex shear moduli

Celltype	R^2 $G'(f)$	R^2 $G''(f)$
A549	0.943	0.954
C2C12	0.943	0.963
CT26	0.965	0.979
HoxB8	0.972	0.960
MCF7	0.963	0.977
MDCK	0.948	0.981
HeLa	0.946	0.987
CB	0.980	0.990
CB + Noc	0.977	0.987
Noc	0.995	0.997

Table 17: R^2-values power law fit of effective energy

Celltype	$R^2 E_{\text{Eff}}(f)$
A549	0.910345
C2C12	0.90804
CT26	0.918026
HoxB8	0.960433
MCF7	0.935251
MDCK	0.934349
HeLa	0.909766
CB	0.965183
CB + Noc	0.575418
HeLa Noc	0.518006

SI 3 Supplementary Figures

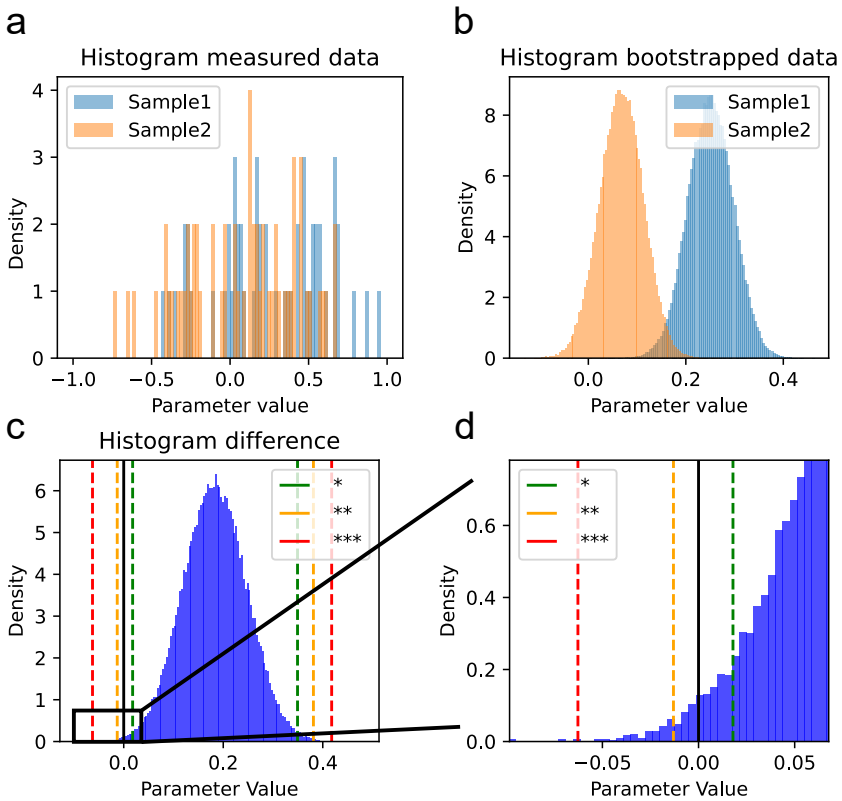

SI Figure 1: Schematic of bootstrapping significance test. a) Histogram for the estimates of two different parameters. b) Bootstrapping procedure was performed on both parameters to get an estimate for the distribution of the mean. c) Difference of both distribution is calculated. d) Depending on which percentile of the distribution is below 0, the significance score is determined

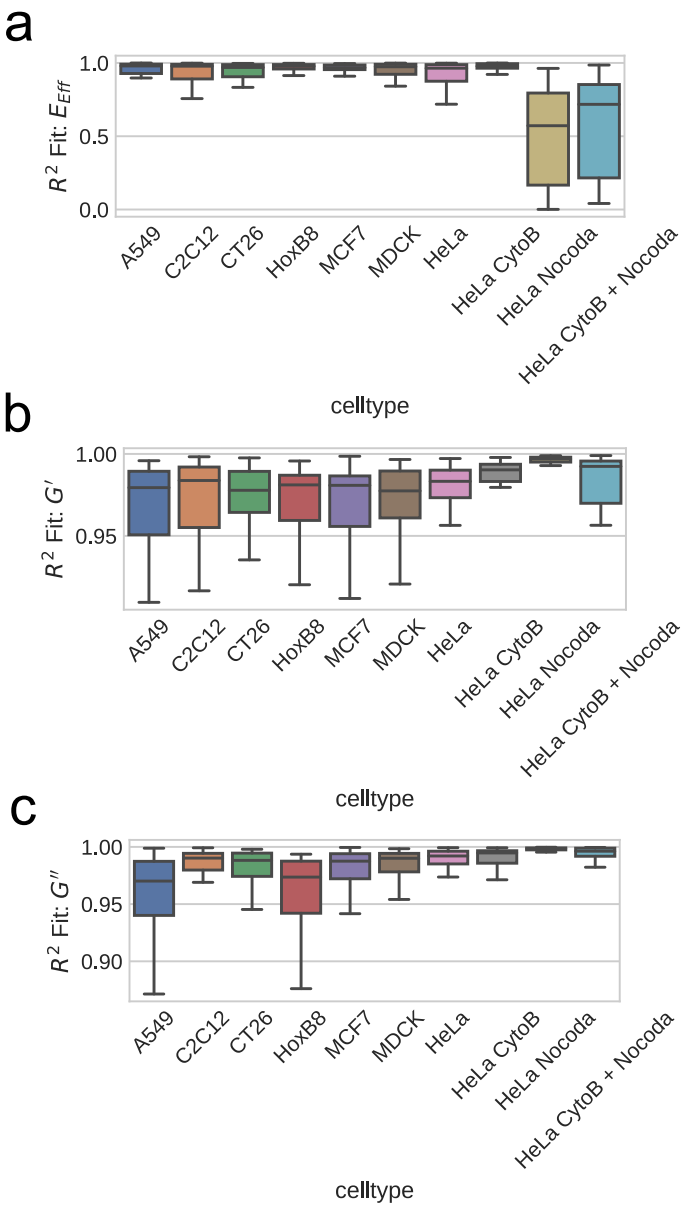

SI Figure 2: R^2-Values for fitting the respective models to a) E_{Eff}, b) $G'(f)$ and c) $G''(f)$

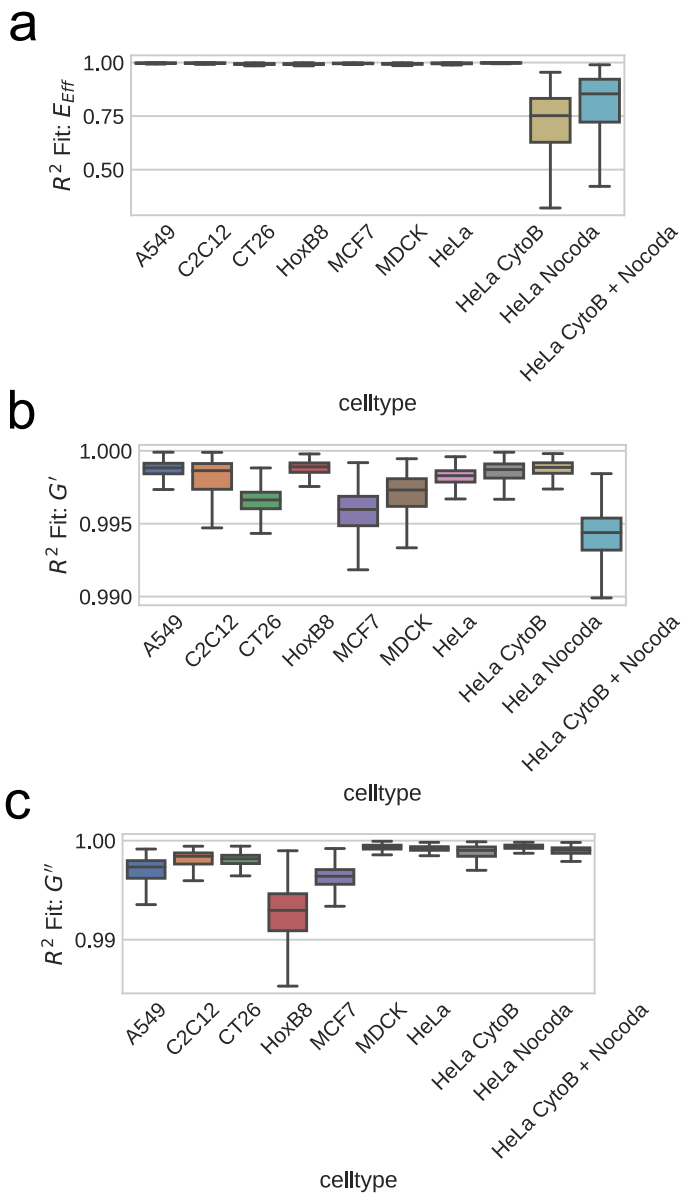

SI Figure 3: R^2-Values for fitting the respective models to the bootstrapped data of a) E_{Eff}, b) $G'(f)$ and c) $G''(f)$